Comparative Evaluation of Physiological and Antimicrobial Properties of Silver Oxide Nanoparticles Synthesized by Plasma Jet

Baydaa Abed Hussein[1], Wahbi Abdulqader Salman[2], Muna Ahmed Issa[3], Sami Salman Chiad[3], Nadir Fadhil Habubi[3, 4, 5] and Yassin Hasan Kadhim[6]

[1]*Department of Biology, Al-Manara College for Medical Sciences, 62001 Amarah, Iraq*
[2]*Department of Biology, College of Science, Al-Turath University, 10013 Baghdad, Iraq*
[3]*Department of Physics, College of Education, Mustansiriyah University, 10052 Baghdad, Iraq*
[4]*Department of Radiation and Sonar Technologies, Alnukhba University College, 10001 Baghdad, Iraq*
[5]*Department of Radiology Techniques, Al-Qalam University College, 36001 Kirkuk, Iraq*
[6]*Department of Optics Techniques, College of Health and Medical Techniques, Al-Mustaqbal University, 51001 Hillah, Iraq*
dr.sami@uomustansiriyah.edu.iq

Keywords: AgO Nanoparticles, Plasma Jet, Antimicrobial Activity, Fungi, Gas Flow Rate, Inhibition Zone, *Candida Albicans*, Staphylococcus Aureus.

Abstract: The structural, optical, and antimicrobial properties of silver oxide (AgO) nanoparticles fabricated by the atmospheric plasma jet method were examined. The nanoparticles were deposited as thin films under variable argon flow rates (0.5, 1.0, and 1.5 L/min) and characterized structurally, morphologically, and optically. X-ray diffraction analysis confirmed polycrystalline films with a preferred (111) crystallographic orientation, with crystallite size increasing from 15.78 to 18.85 nm at elevated flow rates, accompanied by a decline in dislocation density and macrostrain. Atomic force microscopy revealed a reduction in surface roughness and average particle size, suggesting the formation of smoother, more uniform films at higher flow rates. Optical characterization indicated a marginal narrowing of the bandgap from 1.85 to 1.75 eV as the flow rate increased. The antimicrobial efficacy was assessed against Gram-positive bacteria (Staphylococcus aureus, Staphylococcus epidermidis), Gram-negative bacteria (Klebsiella sp., Escherichia coli), and the fungus *Candida albicans* using the agar-well diffusion assay. Gram-positive bacteria demonstrated the greatest susceptibility, with a mean inhibition zone of 27.50 ± 1.64 mm, followed by fungi (25.33 ± 1.53 mm) and Gram-negative bacteria (25.33 ± 2.88 mm). The maximum inhibition zone of 29 mm was recorded for S. aureus at a flow rate of 1.5 L/min.

1 INTRODUCTION

The accelerating prevalence of antimicrobial resistance among pathogenic microorganisms has emerged as a pressing global public health challenge. Conventional antibiotics are progressively declining in therapeutic efficacy owing to the development of resistant bacterial and fungal strains, which has driven the pursuit of alternative antimicrobial agents with enhanced potency and extended activity spectra [1]-[3]. Among the numerous strategies proposed to overcome this challenge, nanotechnology has gained considerable interest due to its capacity to fabricate nanostructured materials with distinctive physicochemical and biological characteristics [4], [5]. The strong antibacterial activity of silver-based nanomaterials, especially silver nanoparticles (AgNPs), against a variety of microorganisms, including fungi and Gram-positive and negative bacteria, has been thoroughly investigated [6]-[8]. The antimicrobial properties of AgNPs are primarily attributed to several well-established mechanisms, including the production of reactive oxygen species (ROS), destabilization of microbial cell membranes, binding to intracellular proteins and genetic material, and impairment of vital metabolic pathways [9]-[11]. These mechanisms collectively result in cellular injury, suppression of microbial proliferation, and ultimately loss of cell viability. Beyond their antimicrobial efficacy, silver nanoparticles have also demonstrated promising interactions with microbial cells at the physiological level, influencing membrane permeability, enzyme function, and intracellular biochemical pathways [12]-[14]. Various fabrication techniques have been developed

for nanoparticle production, broadly classified into chemical, physical, and biological approaches [15]-[17]. Chemical routes include sol-gel [18], chemical reduction [19], and hydrothermal methods [20], whereas physical approaches such as laser ablation [21], sputtering [22], and evaporation-condensation [23] offer elevated purity and accurate regulation of particle formation without requiring chemical reagents [24]. In recent years, plasma-assisted methods have emerged as highly effective routes for synthesizing nanoparticles with tunable dimensions, controlled morphology, and enhanced surface reactivity [25]-[27]. Among these, the atmospheric plasma jet technique has attracted particular interest owing to its operational simplicity, economic viability, and capacity to generate highly reactive plasma species, including reactive oxygen and nitrogen species (RONS), which are essential to both nanoparticle nucleation and antimicrobial processes [28]-[30]. Plasma-assisted fabrication has further demonstrated its ability to enhance the physicochemical properties of nanoparticles, yielding superior antimicrobial performance compared with conventional synthesis routes [31], [32]. Moreover, the interaction between plasma-generated reactive species and metal nanoparticles can produce a synergistic antimicrobial effect, significantly enhancing pathogen elimination [33], [34]. This synergistic mechanism is especially critical when targeting microorganisms with complex cell wall architectures, such as Gram-negative bacteria and fungal species [35], [36]. The physiological response of microbial cells to such treatments encompasses oxidative stress, membrane destabilization, and disruption of essential cellular metabolism [37], [38]. Consequently, the present study aims to examine the physicochemical and antimicrobial performance of AgO nanoparticles fabricated via the atmospheric plasma jet technique against various microbial strains, encompassing Gram-positive and negative bacteria and fungi. Particular emphasis is placed on assessing the impact of plasma operating parameters, notably argon gas flow rate, on the antimicrobial efficacy of the synthesized nanoparticles.

2 EXPERIMENTAL

A non-thermal atmospheric plasma jet setup comprises several essential elements that ensure efficient operation. The neon sign transformer is used as a high-voltage electrical source, in which the rated power is 13 kV and 0.5 mA at an operating frequency of 50 Hz. This transformer lowers total operational expenses by substituting the conventional direct-current power source, which is typically costly. A voltage regulator regulates the input voltage of the high-voltage transformer to maintain efficient operation of the plasma discharge system. The power supply is designed to include overcurrent, open-line, and earth-leakage protection, improving operational stability and safety. The plasma jet configuration consists of dual stainless-steel electrode needles spaced apart by a 2.75 mm Teflon dielectric barrier. The gas flow system ensures controlled gas delivery at the designated flow rate to the plasma via a high-pressure argon reservoir. Gas flow rates range from 0.5 to 2.5 liters per minute, ensuring gas is used in a controlled, optimized manner. A schematic representation of the system is depicted in Figure 1. The plasma jet method was used to produce the nanoparticles, which were then coated onto glass substrates by spin coating to examine their optical and structural properties. This demonstrates that the method can synthesize nanoparticles.

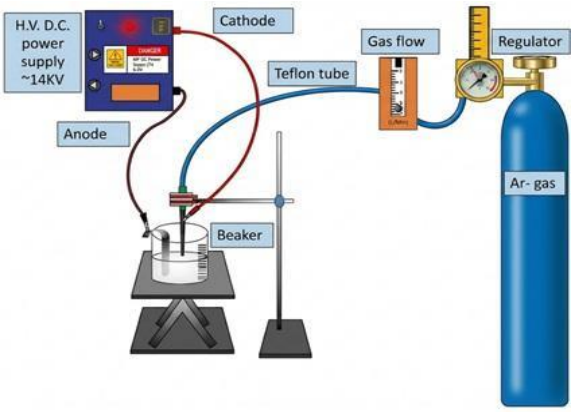

Figure 1: Experimental setup of the atmospheric plasma jet.

Figure 2 illustrates the optical appearance of Ag NPs colloidal suspensions fabricated via plasma-assisted processing at varying argon flow rates. Distinct variations in coloration and opacity are readily observable across the samples, reflecting differences in nanoparticle concentration, size distribution, and colloidal stability. The deeper coloration of certain suspensions is attributed to enhanced nanoparticle yield, owing to more effective plasma-precursor interaction and an elevated generation of reactive species at higher flow rates. Mueller-Hinton agar was freshly prepared, autoclaved, and dispensed into sterile Petri dishes. Bacterial suspensions were uniformly inoculated onto the agar surface using a sterile swab. Antimicrobial

efficacy was subsequently assessed using the agar-well diffusion assay with 6 mm wells, and the diameters of the resulting inhibition zones were recorded after incubation at 37 °C for 24 hours. The structural parameters were determined by XRD (Shimadzu, 6000, Japan) using Cu Kα radiation (λ = 0.15406 nm). The surface morphology of the deposited films was analyzed using AFM (AA 3000 Scanning Probe Microscope). The optical properties were investigated via Cary 100 UV-Visible spectrophotometer.

Figure 2: Plasma-assisted Ag nanoparticle suspensions prepared at different gas flow rates: (1) 0.5 L/min, (2) 1.0 L/min, and (3) 1.5 L/min.

3 RESULTS AND DISCUSSION

Figure 3 presents the X-ray diffraction (XRD) patterns of AgO thin films deposited at argon flow rates of 0.5, 1.0, and 1.5 L/min. All diffraction patterns exhibit well-defined peaks, confirming the polycrystalline nature of the deposited films. The major reflections observed at 34.11°, 37.16°, 52.43°, and 62.22° correspond to the (002), (111), (020), and (220) crystallographic planes, respectively. The diffraction peaks are in good agreement with the standard JCPDS card No. 43-1038, confirming the successful formation of crystalline AgO thin films [15]. Among the observed reflections, the (111) plane exhibits the highest intensity, indicating a preferred crystallographic orientation.

The structural parameters derived from the XRD analysis are summarized in Table 1. The crystallite size increases from 15.78 nm to 16.56 nm and 18.85 nm as the argon flow rate increases from 0.5 to 1.5 L/min. This trend indicates that higher argon flow rates promote crystallite growth during film deposition. The increase in crystallite size is attributed to improved plasma discharge conditions, which enhance adatom surface mobility and facilitate grain coalescence, resulting in larger crystalline domains and fewer grain boundaries [39], [40].

The dislocation density decreases progressively from 62.81×10^{14} to 52.43×10^{14} lines/m² with increasing argon flow rate, indicating a reduction in crystallographic defects and an improvement in the crystalline quality of the deposited films [41], [42]. Similarly, the lattice strain decreases from 29.36×10^{-3} to 22.64×10^{-3} as the argon flow rate increases, suggesting reduced internal stress and enhanced structural ordering resulting from improved atomic arrangement during film growth [43]–[45]. The corresponding structural parameters are summarized in Table 1, while Figure 4 illustrates the variation of FWHM, crystallite size, dislocation density, and lattice strain as a function of argon flow rate.

The surface morphology of the AgO thin films was investigated using atomic force microscopy (AFM), and the corresponding three-dimensional images are presented in Figure 5. All samples were scanned over an area of 2 × 2 µm² and exhibit a homogeneous nanostructured surface with uniformly distributed grains. The extracted AFM parameters are summarized in Table 2. The average particle size decreases from 84.5 nm to 75.0 nm and 62.9 nm as the argon flow rate increases from 0.5 to 1.5 L/min. Likewise, the average surface roughness (Ra) decreases from 7.83 nm to 6.41 nm and 4.28 nm, while the root-mean-square (RMS) roughness decreases from 6.92 nm to 5.41 nm and 4.85 nm. The reduction in particle size and surface roughness indicates that higher argon flow rates improve the uniformity and compactness of the deposited films by enhancing plasma-precursor interactions during the deposition process [46].

Table 1: Structural and optical parameters of AgO thin films.

Gas flow rate (L/min)	2 θ (°)	(hkl) Plane	FWHM (°)	Eg (eV)	*D* (nm)	δ (× 10^{14}) (lines/m^2)	ε (× 10^{-4})
0.5	37.16	111	0.76	1.85	15.78	62.81	29.36
1.0	37.16	111	0.73	1.80	16.56	58.71	26.39
1.5	37.08	111	0.70	1.75	18.85	52.43	22.64

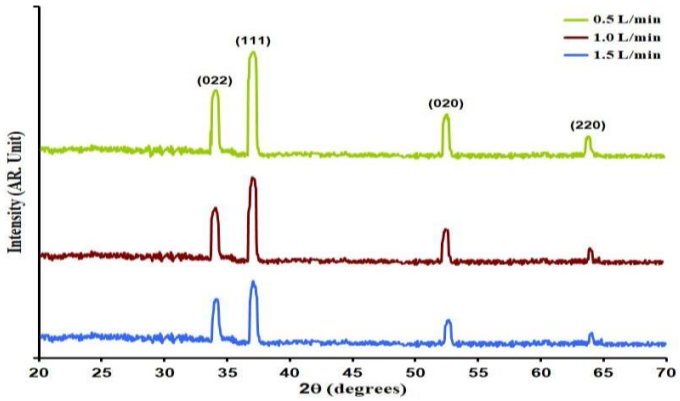

Figure 3: XRD patterns of AgO thin films deposited at different argon flow rates.

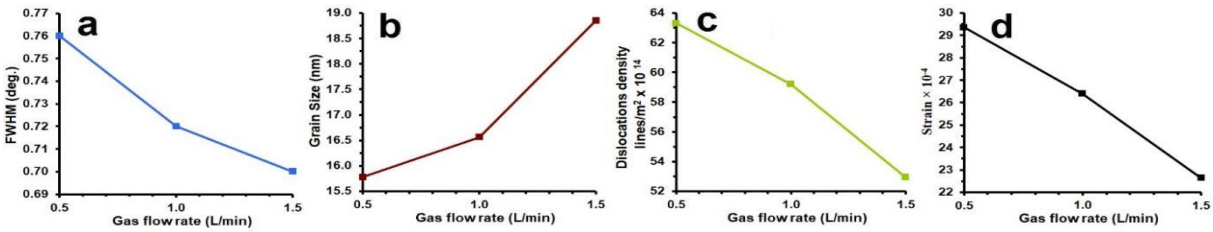

Figure 4: Variation of structural parameters of AgO thin films with argon flow rate: a) FWHM, b) crystallite size (*D*), c) dislocation density (δ), and d) lattice strain (ε).

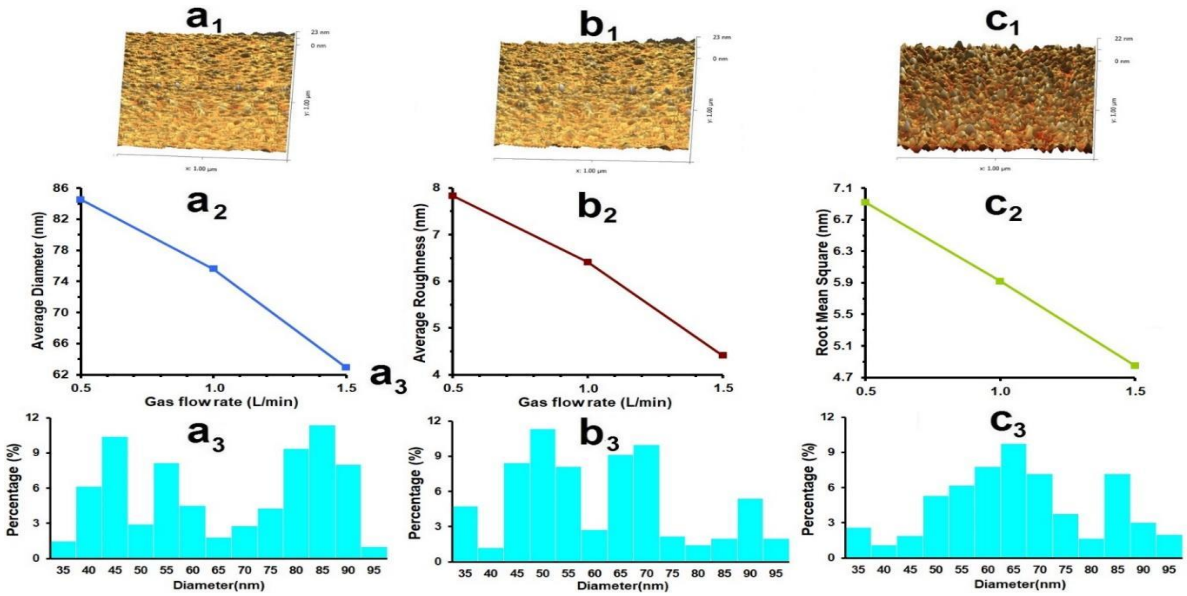

Figure 5: AFM images of AgO thin films deposited at different argon flow rates.

Table 2: AFM parameters of AgO thin films.

Gas flow rate (L/min)	Pav (nm)	R_a (nm)	RMS (nm)
0.5	84.5	7.83	6.92
1.0	75.6	6.41	5.41
1.5	62.9	4.28	4.85

The optical absorbance spectra of the AgO thin films are presented in Figure 6. The absorbance was measured over the wavelength range of 300–900 nm for films deposited at argon flow rates of 0.5, 1.0, and 1.5 L/min. The film prepared at the highest flow rate exhibits the greatest absorbance throughout the investigated spectral range, whereas the film deposited at 0.5 L/min shows the lowest absorbance. The enhanced optical absorption with increasing argon flow rate is attributed to the improved crystallinity, higher film density, and stronger light–matter interaction resulting from enhanced plasma deposition conditions [44], [47]-[49].

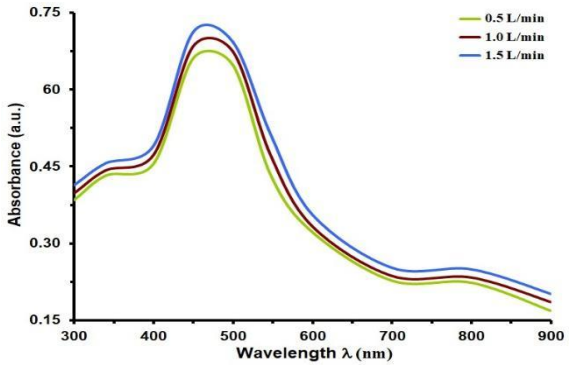

Figure 6: Optical absorbance spectra of AgO thin films deposited at different argon flow rates.

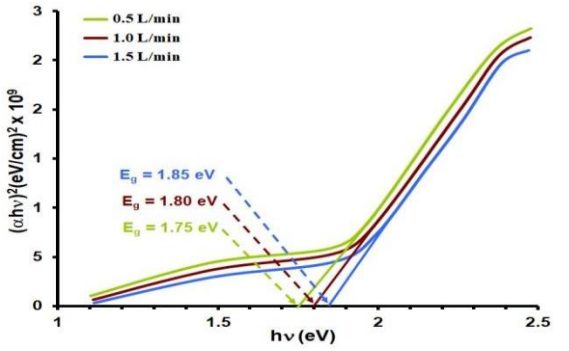

Figure 7: Optical band-gap energy of AgO thin films at different argon flow rates.

The optical band-gap values obtained from the absorption spectra are presented in Figure 7. The band gap decreases gradually from 1.85 eV to 1.80 eV and 1.75 eV as the argon flow rate increases from 0.5 to 1.5 L/min. This gradual narrowing of the band gap is attributed to the increase in crystallite size and the improvement in structural ordering, which modify the electronic states near the valence and conduction bands [50]-[52].

The antimicrobial activity of AgO nanoparticles was evaluated against Gram-positive bacteria, Gram-negative bacteria, and fungal isolates by measuring the inhibition-zone diameters for samples prepared at different argon flow rates (0.5, 1.0, and 1.5 L/min). Figure 8 shows that the Gram-positive bacterial strains *Staphylococcus aureus* and *Staphylococcus epidermidis* exhibit the highest susceptibility to the AgO nanoparticles, as evidenced by the largest inhibition zones. This enhanced sensitivity is attributed to the relatively simple cell-wall structure of Gram-positive bacteria, which lacks an outer membrane and therefore allows easier penetration of silver nanoparticles and plasma-generated reactive species, leading to oxidative stress, disruption of cellular functions, and ultimately cell death [51].

The inhibition zone of *S. aureus* increases from 25 mm at an argon flow rate of 0.5 L/min to 29 mm at 1.5 L/min, indicating that higher argon flow rates enhance the antimicrobial activity of the deposited films. In contrast, *S. epidermidis* exhibits nearly constant inhibition zones of approximately 28–29 mm over the investigated flow-rate range, suggesting that its antimicrobial response is only weakly affected by the deposition conditions [52]–[54]. The corresponding inhibition-zone values are summarized in Table 3.

The average inhibition-zone diameter for the Gram-positive bacteria reaches 27.50 ± 1.64 mm, demonstrating excellent antibacterial activity [55], [56]. The strong antimicrobial performance is attributed to the interaction of AgO nanoparticles and plasma-generated reactive species with the bacterial cell wall, resulting in membrane damage, oxidative stress, and disruption of essential metabolic processes [57], [58].

Figure 9 presents the antibacterial activity against Gram-negative bacteria, including *Escherichia coli* and *Klebsiella* sp. Compared with the Gram-positive strains, these bacteria exhibit smaller and more variable inhibition zones. Their lower susceptibility is mainly attributed to the presence of an outer membrane rich in

lipopolysaccharides, which acts as an effective barrier against the penetration of silver nanoparticles and reactive plasma species [59], [60].

The inhibition zone of *E. coli* decreases from 29 mm to 21 mm as the argon flow rate increases from 0.5 to 1.5 L/min, whereas *Klebsiella* sp. exhibits the largest inhibition zone of 28 mm at an intermediate flow rate of 1.0 L/min. These quantitative results are summarized in Table 3. Statistical analysis presented in Table 4 shows that the Gram-negative bacteria exhibit a lower average inhibition zone (25.33 ± 2.88 mm) together with a larger standard deviation, indicating greater variability in their antimicrobial response [61], [62].

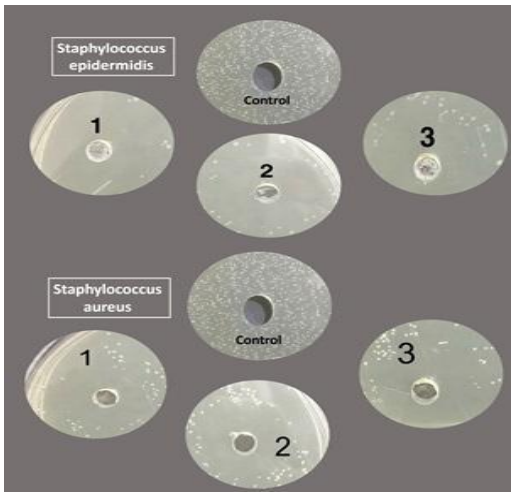

Figure 8: Antibacterial activity of AgO nanoparticles against Gram-positive bacteria at different argon flow rates.

Table 3: Inhibition zone diameters (mm) of Gram-positive bacteria, Gram-negative bacteria, and fungi at different gas flow rates.

Bacteria and Fungi Type		Inhibition zone(mm)		
		0.5 L/min	1 L/min	1.5 L/min
G Positive	S.aureus	25	26	29
	S.epidermidis	28	29	28
G Negative	Klesbsiella sp.	24	28	25

Figure 10 illustrates the antifungal activity of the AgO nanoparticles against *Candida albicans*. The observed inhibition zones confirm the effective suppression of fungal growth and demonstrate the ability of plasma-synthesized AgO nanoparticles to damage fungal cell walls and interfere with essential metabolic processes through the combined action of silver nanoparticles and plasma-generated reactive species [63], [64].

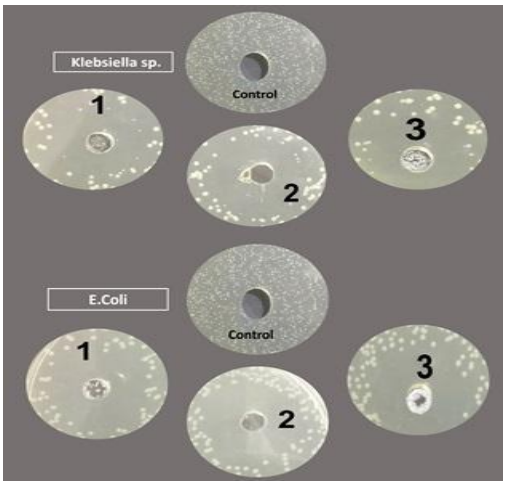

Figure 9: Antibacterial activity of AgO nanoparticles against Gram-negative bacteria at different argon flow rates.

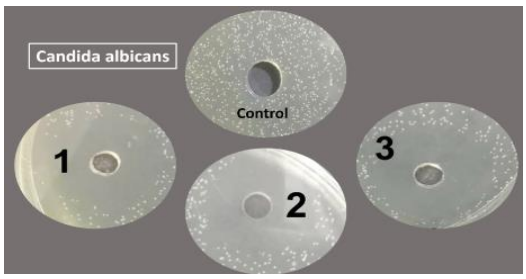

Figure 10: Antifungal activity of AgO nanoparticles against *Candida albicans* at different argon flow rates.

The inhibition zone diameters for *Candida albicans* varied from 24 to 27 mm, with a mean value of 25.33 ± 1.53 mm, indicating a moderate antifungal response, as shown in Tables 3 and 4. The observed differences in inhibition zone size with varying gas flow rates imply that flow rate affects the production and activity of silver nanoparticles and the reactive species generated by plasma, as well as their interactions with the fungal cell wall. The intricate structure of the fungal cell wall, which is mainly composed of chitin and glucans and provides strong defence against external antimicrobial chemicals, is largely responsible for this behaviour [64], [65]. The inhibition zone sizes showed for different gas flow rates are shown graphically in Figure 11 for a more quantitative comparison of antimicrobial activity across various microbial strains. This image shows how gas flow rate affects the effectiveness of silver nanoparticles and the reactive species produced by plasma against bacterial and fungal cells [58].

Table 4: Descriptive statistical analysis (mean ± SD) of inhibition zone diameters for different microbial groups.

Microbial group	Microorganism	0.5 L/min	1 L/min	1.5 L/min	Mean (mm)	SD(mm)
Gram-positive	S. aureus	25	26	29	-	
	S. epidermidis	28	29	28	-	
	Group mean ± SD	-			27.5	1.64
Gram-negative	Klebsiella sp.	24	28	25	-	
	E. coli	29	25	21	-	
	Group mean ± SD	-			25.33	2.88
Fungi	*Candida albicans*	25	24	27	25.33	1.53

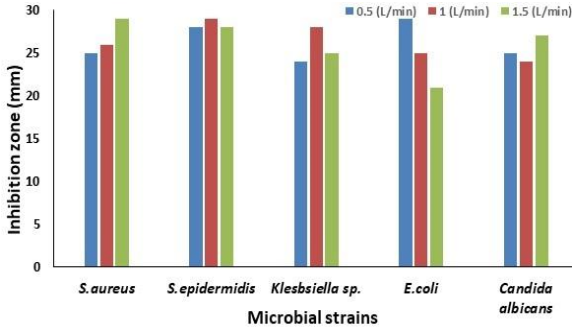

Figure 11: Inhibition zone diameters of microbial strains treated with plasma-assisted AgO nanoparticles at different argon flow rates.

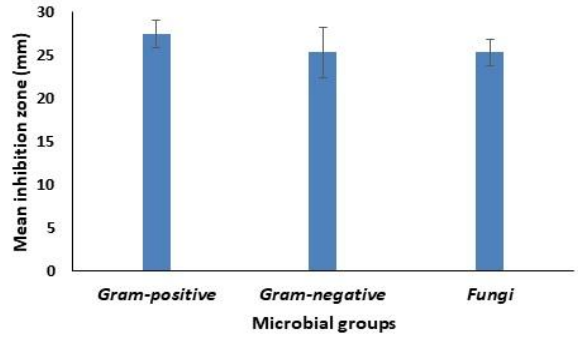

Figure 12: Mean inhibition zone diameters (mean ± SD) for Gram-positive bacteria, Gram-negative bacteria, and fungi treated with plasma-assisted AgO nanoparticles.

Gram-positive bacteria had the largest mean inhibition zone, followed by fungi, while Gram-negative bacteria had the smallest mean inhibition zone and the greatest variability, according to the descriptive statistical analysis of inhibition zone diameters, summarised in Table 4 and illustrated in Figure 12. This pattern reflects inherent differences in microbial cell structure: Gram-positive bacteria's lack of an outer membrane increases their susceptibility to plasma-generated reactive species and nanoparticles of silver, while Gram-negative bacteria's outer membrane functions as a barrier that limits the effectiveness of antibiotics. The complex composition of fungi's cell walls, which are mostly composed of chitin and glucans, is thought to be responsible for their intermediate response, as it partially limits the efficacy of antimicrobial drugs [66].

4 CONCLUSIONS

In this work, we demonstrate that the plasma jet technique can be used to produce AgO nanoparticles with tunable structures, optical properties, and antimicrobial activity. The gas flow rate used in the synthesis is highly relevant to determining the physicochemical properties of the nanoparticles. Higher flow rates lead to larger crystallite sizes, lower lattice strain and dislocation density, and a smoother surface shape, ultimately increasing the performance of the films in resisting more microbes. The antimicrobial study shows that the AgO nanoparticles are highly active against the entire class of microorganisms. Gram-positive bacteria showed a stronger antigenic response in this manner due to their simpler cell wall structure, whereas Gram-negative bacteria were less sensitive (due to the shield) because of the protection provided by the cell wall. The fungal strain *Candida albicans* had a moderate, flow-rate-dependent response. The best effectiveness of antimicrobial agents was obtained at 1.5 L/min, and a successful strategy of synthesis for the bacteria must therefore be considered. The combination of reactive oxygen and nitrogen in plasma and silver in nanoparticles for bacterial inflammation led to microbial inactivation due to oxidative stress, membrane modification, and negative interaction of cells with the cells.

ACKNOWLEDGMENTS

The authors acknowledge the financial support provided by Mustansiriyah University, Baghdad, Iraq (www.uomustansiriyah.edu.iq), and Al-Nukhba University College.

REFERENCES

[1] S. Rodrigues, J. G. S. Batista, M. A. V. Rodrigues, V. C. Thipe, L. A. R. Minarini, P. S. Lopes, and A. B. Lugão, "Advances in silver nanoparticles as antimicrobial agents and their mechanisms of action," Frontiers in Microbiology, vol. 15, 1440065, 2024.

[2] H. Jangid, S. Singh, P. Kashyap, A. Singh, and G. Kumar, "Biomedical applications of silver nanoparticles in antimicrobial and wound healing therapies," Frontiers in Pharmacology, vol. 15, 1438227, 2024.

[3] I. Shaikh, S. Shafi, A. Kazi, R. Sante, A. Jadhav, G. Mohini, and P. Ritthe, "Silver nanoparticles as a modern era antimicrobial agent," Asian Journal of Pharmaceutical Research and Development, vol. 12, pp. 144-149, 2024.

[4] M. R. Gheni and N. H. Odaa, "Antimicrobial activity of silver nanoparticles against urinary tract pathogens," Ibn Al-Haitham Journal for Pure and Applied Sciences, vol. 37, pp. 119-128, 2024.

[5] M. S. Tareq, A. K. Hameed, A. H. Saleem, and B. G. Rasheed, "In vitro antimicrobial activity of laser-synthesized silver nanoparticles," Lasers in Medical Science, vol. 40, p. 271, 2025.

[6] P. Singh, Y. J. Kim, D. Zhang, and D. C. Yang, "Biological synthesis of nanoparticles and their applications," Trends in Biotechnology, vol. 38, pp. 123-134, 2020.

[7] X. F. Zhang, Z. G. Liu, W. Shen, and S. Gurunathan, "Silver nanoparticles: synthesis, characterization and biomedical applications," International Journal of Molecular Sciences, vol. 21, p. 1534, 2020.

[8] Y. N. Slavin, J. Asnis, U. O. Häfeli, and H. Bach, "Metal nanoparticles as antimicrobial agents," Journal of Nanobiotechnology, vol. 18, p. 65, 2020.

[9] N. Durán, M. Durán, M. B. de Jesus, et al., "Silver nanoparticles: mechanistic aspects of antimicrobial activity," Nanomedicine, vol. 15, pp. 789-799, 2020.

[10] S. Prabhu and E. K. Poulose, "Silver nanoparticles: mechanism of antimicrobial action," International Nano Letters, vol. 10, pp. 1-10, 2020.

[11] S. M. Dizaj, F. Lotfipour, M. Barzegar-Jalali, et al., "Antimicrobial activity of metal oxide nanoparticles," Materials Science and Engineering C, vol. 118, pp. 111-118, 2021.

[12] M. G. Kong, G. Kroesen, G. Morfill, et al., "Plasma medicine: applications of cold atmospheric plasma in biology and medicine," New Journal of Physics, vol. 23, 115012, 2021.

[13] D. B. Graves, "Reactive oxygen and nitrogen species in plasma medicine," Journal of Physics D: Applied Physics, vol. 54, 263001, 2021.

[14] G. Fridman, G. Friedman, A. Gutsol, et al., "Applied plasma medicine," Plasma Processes and Polymers, vol. 18, e2000231, 2021.

[15] A. Vinukonda, N. Bolledla, R. K. Jadi, R. Chinthala, and V. R. Devadasu, "Synthesis of nanoparticles using advanced techniques," Next Nanotechnology, vol. 8, 100169, 2025.

[16] N. Al-Harbi and N. K. Abd-Elrahman, "Physical methods for preparation of nanomaterials, their characterization and applications: a review," Journal of Umm Al-Qura University for Applied Sciences, vol. 11, no. 2, pp. 356-377, 2025.

[17] D. Kirubakaran, J. B. A. Wahid, N. Karmegam, R. Jeevika, L. Sellapillai, M. Rajkumar, and K. J. SenthilKumar, "A comprehensive review on the green synthesis of nanoparticles: advancements in biomedical and environmental applications," Biomedical Materials & Devices, vol. 4, no. 1, pp. 388-413, 2026.

[18] A. R. Chavan, S. B. Bhosale, S. B. Somvanshi, and P. P. Khirade, "Effect of Zr4+ dopants on micro-structural and antibacterial characteristics of CuFe2O4 nanoparticles produced via sol-gel auto combustion," Journal of Sol-Gel Science and Technology, vol. 116, no. 1, pp. 434-447, 2025.

[19] Pricop, A. Negrea, B. Pascu, N. S. Nemeş, M. Ciopec, P. Negrea, et al., "Copper nanoparticles synthesized by chemical reduction with medical applications," International Journal of Molecular Sciences, vol. 26, no. 4, p. 1628, 2025.

[20] S. Ahmad, H. Ni, F. S. Al-Mubaddel, M. A. Rizk, M. B. Ammar, A. U. Khan, et al., "Magnetic properties of different phases iron oxide nanoparticles prepared by micro emulsion-hydrothermal method," Scientific Reports, vol. 15, no. 1, p. 878, 2025.

[21] M. A. Issa and K. A. Aadim, "Activity of (ZnO: NiO) nanoparticles prepared by plasma jet and pulse laser deposition (PLD) techniques against Staphylococcus aureus, Staphylococcus epidermidis, Klebsiella species, Escherichia coli and *Candida albicans*," in AIP Conference Proceedings, vol. 3415, no. 1, p. 030004, 2026.

[22] M. Xiao, Z. Song, X. Gao, S. Yang, X. Hui, X. Du, et al., "Regulation of the surface morphology of CoNiSe2 by magnetron sputtering of Au nanoparticles for the property-promotion of electrode materials for high-performance supercapacitors," Journal of Alloys and Compounds, vol. 1035, 181452, 2025.

[23] P. S. Pawar, S. M. Ahire, V. V. Shewale, S. Jadhav, S. K. Mahajan, and D. D. Sonawane, "Silver Nanoparticles: A Comprehensive Review on Synthesis, Properties and Applications," Research Journal of Pharmaceutical Dosage Forms and Technology, vol. 17, no. 4, pp. 279-285, 2025.

[24] J. H. Swisher, L. Jibril, S. H. Petrosko, and C. A. Mirkin, "Nanoreactors for particle synthesis," Nature Reviews Materials, vol. 7, no. 6, pp. 428-448, 2022.

[25] J. E. Foster, B. S. Sommers, S. N. Gucker, et al., "Plasma-liquid interactions for antimicrobial treatment," IEEE Transactions on Plasma Science, vol. 49, pp. 1311-1323, 2021.

[26] S. Iravani and R. S. Varma, "Green synthesis of metal nanoparticles using plants," Green Chemistry, vol. 24, pp. 1179-1202, 2022.

[27] M. Rai, S. Deshmukh, A. Ingle, et al., "Silver nanoparticles as antimicrobial agents against multidrug-resistant bacteria," Journal of Applied Microbiology, vol. 132, pp. 1234-1245, 2022.

[28] T. Ahmad, I. A. Wani, I. H. Lone, et al., "Antifungal activity of silver nanoparticles," Colloids and Surfaces B: Biointerfaces, vol. 208, pp. 112-119, 2022.

[29] M. Issa and K. A. Aadim, "Influence of gas flow rate on the plasma temperature and electron density of an atmospheric argon plasma jet," Jordan Journal of Physics, vol. 18, no. 4, pp. 435-442, 2025.

[30] V. K. Sharma, R. A. Yngard, and Y. Lin, "Silver nanoparticles: green synthesis and antimicrobial properties," Advances in Colloid and Interface Science, vol. 298, pp. 102-110, 2022.

[31] K. M. Abou El-Nour, A. Eftaiha, A. Al-Warthan, and R. A. Ammar, "Synthesis and biomedical applications of silver nanoparticles," Arabian Journal of Chemistry, vol. 15, pp. 103-112, 2022.

[32] G. Primc, K. Brenčič, M. Mozetič, and M. Gorjanc, "Recent advances in the plasma-assisted synthesis of zinc oxide nanoparticles," Nanomaterials, vol. 11, no. 5, p. 1191, 2021.

[33] P. Lukes, V. Babicky, M. Clupek, et al., "Plasma technologies for microbial inactivation in water treatment," Chemical Engineering Journal, vol. 452, pp. 139-148, 2023.

[34] M. A. Issa and K. A. Aadim, "Study the structural and optical properties of Zinc Oxide prepared by pulse laser deposition," J Opt, vol. 55, pp. 755-760, 2026.

[35] Y. K. Mohanta and S. K. Behera, "Biosynthesis of silver nanoparticles and antimicrobial activity against pathogens," Applied Microbiology and Biotechnology, vol. 107, pp. 233-242, 2023.

[36] S. Ahmed, M. Ahmad, B. L. Swami, and S. Ikram, "Green synthesis of silver nanoparticles using plant extracts," Journal of Radiation Research and Applied Sciences, vol. 16, pp. 100-108, 2023.

[37] K. K. Rajak, P. Pahilani, H. Patel, et al., "Green synthesis of silver nanoparticles using plant extract and antibacterial activity," Materials Today Communications, vol. 35, pp. 105-110, 2023.

[38] R. Singh and D. Singh, "Antibacterial properties of silver nanoparticles in biomedical applications," Nanotechnology Reviews, vol. 12, pp. 189-202, 2023.

[39] R. R. Ahmed, T. H. Mubarak, and I. H. Mohamed, "A study of structural and chemical properties of Ni1-xZnxFe2O4 ferrite powder prepared by co-precipitation method," Digest Journal of Nanomaterials and Biostructures, vol. 17, no. 3, pp. 741-748, 2022.

[40] A. A. Khadayeir, R. I. Jasim, S. H. Jumaah, N. F. Habubi, and S. S. Chiad, "Influence of substrate temperature on physical properties of nanostructured ZnS thin films," Journal of Physics: Conference Series, vol. 1664, no. 1, p. 012009, 2020.

[41] M. B. Jumaa, T. H. Mubarak, and A. M. Mohammad, "Synthesis and Characterization of Spinel Ferrite Co0.8Fe2.2O4 Nanoparticle," Journal of University of Anbar for Pure Science, vol. 15, no. 2, pp. 74-82, 2021.

[42] S. S. Chiad, A. S. Alkelaby, and K. S. Sharba, "Optical conduct of nanostructure Co3O4 rich highly doping Co3O4: Zn alloys," Journal of Global Pharma Technology, vol. 11, no. 7, pp. 662-665, 2020.

[43] R. Kuekha, T. H. Mubarak, and B. Azhdar, "Synthesis, structural, magnetic, and dielectric properties of Ni2+, Mn2+ Co-substituted CoFe2O4 nanoferrites using sol-gel auto combustion method," Materials Science and Engineering B, vol. 292, 116411, 2023.

[44] R. S. Mohammed and M. F. Al-Marjani, "Plasma-solution interaction as green pathway to synthesize novel hybrid nanoparticles for medical sterilization (catheter sterilization)," The European Physical Journal Plus, vol. 140, no. 2, p. 156, 2025.

[45] L. Nadjia and E. Abdelkader, "Design, synthesis and characterization of ceria: assessment of crystallite size and intrinsic strain using XRD profile analysis and its photocatalytic applications," Journal of the Iranian Chemical Society, vol. 22, no. 2, pp. 297-324, 2025.

[46] J. Wang, P. Ni, C. Chen, M. Ersson, and Y. Li, "Effect of gas blowing nozzle angle on multiphase flow and mass transfer during RH refining process," International Journal of Minerals, Metallurgy and Materials, vol. 30, no. 5, pp. 844-856, 2023.

[47] T. H. Mubarak, K. H. Hassan, and Z. M. A. Abbas, "Using X-ray diffraction and scanning electron microscope to study zinc oxide nanoparticles prepared by wet chemical method," Advanced Materials Research, vol. 685, pp. 119-122, 2013.

[48] R. Kuekha, T. H. Mubarak, and B. Azhdar, "Electromagnetic interference shielding and characterization of Ni2+ substituted cobalt nanoferrites prepared by sol-gel auto combustion," Advances in Materials Science and Engineering, vol. 2022, Art. no. 3992402, 2022.

[49] D. M. Shaker, R. R. Ahmed, A. M. Mohammad, T. H. Mubarak, and I. H. Mohamed, "Synthesis and characterization of CoZnFe2O4 ferrite nanoparticles by co-precipitation method for biomedical applications," Passer Journal of Basic and Applied Sciences, vol. 6, no. 2, pp. 488-493, 2024.

[50] S. Kumar and A. Pandey, "Mechanisms of antimicrobial action of silver nanoparticles," Journal of Nanobiotechnology, vol. 22, pp. 121-130, 2024.

[51] M. Hassan and M. Khan, "Plasma-assisted synthesis of metal nanoparticles for biomedical applications," Applied Surface Science, vol. 646, pp. 158-166, 2024.

[52] Y. Wang, X. Li, and L. Chen, "Antimicrobial activity of metal nanoparticles against bacterial pathogens," Nano Research, vol. 17, pp. 223-235, 2024.

[53] I. Khan, K. Saeed, and I. Khan, "Nanoparticles: properties, applications and toxicity," Arabian Journal of Chemistry, vol. 17, pp. 104-115, 2024.

[54] R. Gupta and P. Sharma, "Silver nanoparticle-mediated antimicrobial therapy," International Journal of Nanomedicine, vol. 19, pp. 105-118, 2024.

[55] A. Ali and M. Abbas, "Plasma jet technology for synthesis of antimicrobial nanoparticles," Plasma Chemistry and Plasma Processing, vol. 44, pp. 879-892, 2024.

[56] H. Ali and N. Ahmed, "Silver nanoparticle-based antifungal therapy against *Candida albicans*," Journal of Fungi, vol. 11, pp. 245-256, 2025.

[57] S. Khan and A. Rahman, "Plasma-synthesized nanoparticles for biomedical applications," Materials Letters, vol. 371, pp. 132-140, 2025.

[58] N. Roustaei, "Application and interpretation of linear-regression analysis," Medical Hypothesis, Discovery and Innovation in Ophthalmology, vol. 13, no. 3, p. 151, 2024.

[59] S. A. Benseghier, F. Bennabi, I. Ercan, H. Nehmar, Y. Khane, N. Moulayat, et al., "Low-Cost synthesis of Ag-doped NiO thin Films: Their structural, optical, photocatalytic and antimicrobial properties," Inorganic Chemistry Communications, vol. 159, 111787, 2024.

[60] J. M. Rzaij, Q. A. Abbas, and A. M. Khalaf, "Investigating the structural, topographical, morphological and optical effects of AgO on sprayed SnO2 thin films," Bulletin of Materials Science, vol. 46, no. 4, p. 200, 2023.

[61] Y. Zidane, S. E. Laouini, A. Bouafia, S. Meneceur, M. L. Tedjani, S. A. Alshareef, et al., "Green synthesis of multifunctional MgO@AgO/Ag2O nanocomposite for photocatalytic degradation of methylene blue and toluidine blue," Frontiers in Chemistry, vol. 10, 1083596, 2022.

[62] A. Rita, A. Sivakumar, S. S. J. Dhas, and S. M. B. Dhas, "Structural, optical and magnetic properties of silver oxide (AgO) nanoparticles at shocked conditions," Journal of Nanostructure in Chemistry, vol. 10, no. 4, pp. 309-316, 2020.

[63] L. He, H. Kang, G. Hou, X. Qiao, X. Jia, W. Qin, and X. Wu, "Low-temperature synthesis of nano-porous high entropy spinel oxides with high grain boundary density for oxygen evolution reaction," Chemical Engineering Journal, vol. 460, 141675, 2023.

[64] J. Li, K. Li, Z. Li, C. Wang, Y. Liang, Y. Pang, et al., "Capture of single Ag atoms through high-temperature-induced crystal plane reconstruction," Nature Communications, vol. 15, no. 1, p. 3874, 2024.

[65] W. R. Talib, A. Sudhakaran, A. Sudhakaran, and R. S. Mohammed, "Potential biological and optoelectronic applications of AgO: ZnO nanocomposite synthesized by green approach," The European Physical Journal Plus, vol. 139, no. 12, p. 1118, 2024.

[66] R. O. Trevisan, J. M. Oliveira, H. F. Perini, U. Travaglini, T. K. D. L. Rezende, F. R. dos Santos, et al., "Enhanced antibacterial efficacy of biocompatible Ag-doped ZnO/AgO/TiO2 nanocomposites against multiresistant bacteria," Next Materials, vol. 7, 100447, 2025.